Nano Research
2022, 15(9): 7917–7924

ISSN 1998-0124 CN 11-5974/O4
https://doi.org/10.1007/s12274-022-4448-6

Research Article

Metal-organic framework-derived Co nanoparticles and single atoms as efficient electrocatalyst for pH universal hydrogen evolution reaction

Rui jiang[1,§], Qian Li[1,§], Xue Zheng[1], Weizhe Wang[1], Shuangbao Wang[1], Zhimou Xu[1] (✉), and Jiabin Wu[2] (✉)

[1] *School of Optical and Electronic Information, Huazhong University of Science and Technology (HUST), Wuhan 430074, China*
[2] *Department of Chemistry, Tsinghua University, Beijing 100084, China*
[§] *Rui jiang and Qian Li contributed equally to this work.*

Received: 26 February 2022 / **Revised:** 14 April 2022 / **Accepted:** 20 April 2022

ABSTRACT

Hydrogen release through water splitting is essential for reducing carbon emissions and promoting the hydrogen economy. One of the crucial challenges for industrial applications of water electrolysis is the manufacture of electrocatalysts which can reduce the kinetic energy barrier of the hydrogen evolution reaction (HER). Loading transition metal (TM) nanoparticles (NPs) or single atoms (SAs) into heteroatom-doped carbon materials (HCMs) is an effective method to improve electrochemical activity and stability. To this end, we synthesized N-doped porous carbon (NC) encapsulated Co NPs and isolated Co SA nanocatalysts (denoted as Co NPs@SAs-NC) using metal-organic frameworks (MOFs) as sacrificial precursors. The Co NPs@SAs-NC nanocatalysts displayed outstanding HER activity with a 110 mV overpotential in 1 M KOH, 47 mV overpotential in 0.5 M H_2SO_4 and 171 mV in 0.5 M phosphate-buffered saline (PBS) to reach a current density of 10 mA·cm^{-2}. In addition, the mechanism of the synergistic effect of Co NPs, Co SAs and N species was investigated in-depth using *in situ* shielding experiments and density functional theory (DFT) calculations.

KEYWORDS

metal-organic frameworks, hydrogen evolution reaction, nanocatalysts, single atoms, pH universal

1 Introduction

To meet the goals of reducing carbon dioxide emissions and achieving carbon neutrality, clean and sustainable energy sources should be urgently employed as substitutes for fossil energy [1]. Hydrogen energy is one of the most promising candidates for sustainable energy sources owing to its high calorific value and abundant reserves [2–4]. Electrochemical water splitting ($2H_2O \rightarrow 2H_2 + O_2$) is an attractive method for converting intermittent energy (e.g., solar, wind, and geothermal energies) to storable hydrogen energy [5, 6]. However, the practical use of water electrolysis is not feasible due to the sluggish reaction kinetics [7]. Among the reported catalysts, noble metals (e.g., Pt and Ru) have shown excellent hydrogen evolution reaction (HER) activity [8–12]. However, their commercial applications are restricted by their scarcity and cost. Therefore, the development of non-noble metal HER catalysts is necessary for the industrial application of water electrolysis.

First-row transition metals (TMs) (e.g., Fe, Co, and Ni) as well as their alloys, sulfides, phosphides, and nitrides exhibit competitive HER activities [13–20]. The strategy of encapsulating TM-based catalysts in carbon shells has been frequently employed to improve the catalytic activity and stability of electrocatalysts [21, 22]. The carbon shells not only inhibit the migration of the catalysts but also protect them from corrosion during the electrochemical process [23, 24]. In addition, the high porosity and large surface area of the carbon shells facilitate the exposure of the active centers and local accessibility of the electrolytes [25]. Furthermore, the single atoms bonded with the heteroatoms (especially N atoms) in carbon shells have been reported to modify the electronic structures and optimize the adsorption capacity to the intermediate, which is beneficial for electrochemical reactions [26–30]. However, the Co–N_x single atom (SA) catalysts have been rarely reported for efficient HER performance in alkaline solution due to the sluggish process of water adsorption on TM SA surface. Co-based nanoparticles (NPs) have received considerable attention as alkaline HER catalysts owing to their low Gibbs free energy toward HER [13, 24]. However, the high energy barrier of water dissociation on the Co NPs surface limits its application [31, 32]. Hitherto, the synergic effect between the NPs and SAs in NC materials has not been reported to improve the HER activity [33, 34].

Owing to the high porosity, large surface area, and ultrahigh density of exposed metal ions, metal-organic frameworks (MOFs) have drawn considerable attention as sacrificial precursors for the synthesis of the TM/C composites [35, 36]. The organic ligands can be converted to heteroatom-doped carbon material (HCM), and the TM ions can be reduced by carbon through the carbonization process. In addition, the isolating effect of the TM SAs to NPs can directly minimize the aggregation and enrich the active sites [11]. Based on the above considerations, we suggested a

Address correspondence to Zhimou Xu, Xuzhimou@hust.edu.cn; Jiabin Wu, jiabinwu@tsinghua.edu.cn

simple thermal treatment for synthesis of Co NPs@SAs-NC (NC = N-doped porous carbon) electrocatalyst featuring Co NPs and SAs-doped NC. The Co NPs@SAs-NC catalyst exhibited outstanding HER activity in both acidic and alkaline media, with extraordinary long-term durability. Both poor activities of the Co NPs-NC and Co SAs-NC established the indispensability of the Co NPs and Co SAs. The results of electrochemical performances and density functional theory (DFT) calculations reveal that the co-existence of the Co NPs, Co SAs and N species is responsible for the outstanding HER catalytic activity.

2 Experimental section

2.1 Synthesis of ZIF-67

All solvents and chemicals were purchased from commercial supplies and used without further purification (Section S1 in the Electronic Supplementary Material (ESM)). $Co(NO_3)_2{\cdot}6H_2O$ (4.365 g, 15 mmol) and 2-methylimidazole ($C_4H_6N_2$, 4.926 g, 60 mmol) were dissolved in a binary mixture of EtOH (120 mL, 2.064 mol) and methanol (120 mL, 2.823 mol). Upon mixing the two solutions under vigorous stirring (1,000 rpm) for 30 s, a purple suspension was obtained, which was kept undisturbed at room temperature. After 24 h, the mother solution was filtered, and the obtained purple solid was washed three times with methanol (500 mL) over 3 d to remove the residue. Finally, the suspension was filtered to obtain ZIF-67 powder, which was dried overnight at 60 °C under vacuum.

2.2 Synthesis of Co NPs@SAs-NC

The ZIF-67 powder (200 mg) was calcined in a tube furnace at 850 °C for 6 h at a heating rate of 5 °C·min^{-1} under an N_2 atmosphere via an isothermal process at 500 °C for 2 h. The product was etched with 1 M H_2SO_4 for 4 h at room temperature, followed by filtration and washing with water and methanol. The obtained products were named Co NPs@SAs-NC.

2.3 Synthesis of Co NPs-NC, Co SAs-NC and NC

For comparison, Co NPs-NC was prepared by carbonizing ZIF-67 powder at 850 °C for 6 h at a heating rate of 5 °C·min^{-1} under the N_2 atmosphere in a tube furnace without isothermal process. The Co SAs-NC was prepared via acid etching of Co NPs@SAs-NC in H_2SO_4 solution (1 M) at 80 °C for 24 h. The NC was prepared by acid etching of Co NPs-NC in the H_2SO_4 solution (1 M) at 80 °C for 24 h.

2.4 Preparation of working electrodes

A glassy carbon electrode (GCE, 5 mm diameter) was polished with 1,000, 300, and 50 nm alumina suspensions to obtain a mirror-like surface, and then cleaned ultrasonically in the presence of nitric acid (HNO_3, 1 M), acetone (C_3H_6O), and deionized water. The catalyst ink was composed of a catalyst (5 mg), ethanol (860 μL), water (100 μL), and Nafion solution (40 μL, 5 wt.%) which were mixed ultrasonically for 30 min. To prepare the working electrode, the ink (12 μL) was drop-casted onto the surface of the clean GCE and dried in air (catalyst loading: 0.306 mg·cm^{-2}).

2.5 Electrochemical measurements

The electrochemical properties of all the catalysts were measured using a CHI 760e electrochemical workstation (CH Instruments Corp., Ltd.) using a three-electrode system at 25 °C. A carbon rod served as the counter electrode, while Ag/AgCl and Hg/HgO electrodes were used as reference electrodes in the linear sweep voltammetry (LSV) and cyclic voltammetry (CV) tests, respectively. The electrolytes were KOH solution (1 M, pH = 13.8), H_2SO_4 solution (0.5 M, pH = 0.3) and phosphate-buffered saline (PBS) solution (0.5 M, pH = 7.0), and the electrolyte solution was bubbled by N_2 for 2 h to remove dissolved oxygen before tests. The LSV tests were performed at a scan rate of 5 mV·s^{-1} to obtain the polarization curves, and the overpotentials were calculated according to the Nernst equation

$$E_{RHE} = E_{Hg/HgO} + 2.303RT/F \cdot pH + E^0_{HgO/Hg}(\text{alkaline solution}) = E_{Hg/HgO} + 0.9122$$

$$E_{RHE} = E_{Ag/AgCl} + 2.303RT/F \cdot pH + E^0_{Ag/AgCl}(\text{acid solution}) = E_{Ag/AgCl} + 0.2223$$

$$E_{RHE} = E_{Ag/AgCl} + 2.303RT/F \cdot pH + E^0_{Ag/AgCl}(\text{neutral solution}) = E_{Ag/AgCl} + 0.6176$$

Tafel slopes of the electrocatalysts were calculated by fitting the polarization curve by using the Tafel equation ($\eta = b\log j + a$, where b is the Tafel slope; j is the current density; η is the overpotential). Long-term stability was measured using the CV tests method over 1,000 cycles at a scan rate of 100 mV·s^{-1} between −100 and 300 mV (vs. RHE) and chronopotentiometry at a current density of 10 mA·cm^{-2} for 24 h. The electrochemically active surface area (ECSA) was analyzed by testing the double layer capacitances (C_{dl}). And the C_{dl} values of catalysts were studied by CVs with varied scanning rates from 10 to 50 mV·s^{-1}. The regions of potential were set at −0.1–0 V for 1 M KOH, 0–0.1 V for 0.5 M H_2SO_4 and 0–0.1 V for 0.5 M PBS because no obvious electrochemical features corresponding to the Faradic current were observed.

3 Results and discussion

3.1 Characterization of catalysts

The well-defined nanostructured ZIF-67 was constructed according to a previous report [37]. Subsequently, as shown in Fig. 1, the ZIF-67 powder was calcined in a tube furnace at 850 °C for 6 h via an isothermal process at 500 °C to obtain the Co NPs@SAs-NC nanocatalyst. The thermogravimetric analysis (TGA) curve (Fig. S1 in the ESM) exhibits a two-step weight loss over 100–1,000 °C. Stage one (< 480 °C) represents the evaporation of the physically adsorbed solvents, and stage two (480–1,000 °C) constitutes the carbonization of the organic ligands. It should be noted that the initial isothermal process at 500 °C is important, in this process ZIF-67 would laggingly release heteroatoms to form the defect sites which can capture the Co SAs; then in higher temperature, partial cobalt atoms would aggregate into large Co NP [38, 39]. Furthermore, the subsequent high-temperature carbonization process facilitates the tuning of conductivity and N doping of porous carbon materials [40]. For comparison, we prepared samples of ZIF-67 carbonized in one step at 850 °C without an isothermal process. As shown in the X-ray diffraction (XRD) patterns (Fig. S2 in the ESM), the diffraction peaks located at 44.2° and 51.5° are consistent with Co (PDF#15-0806), demonstrating the formation of Co NPs after calcination of ZIF-67 at 850 °C. In addition, the diffraction peak observed at 26.1° is originated from the hexagonal graphitic structure of graphene carbon. In the Raman spectrum (Fig. S3 in the ESM), the unambiguous peaks at 1,355 and 1,580 cm^{-1} correspond to the disordered sp^3 carbon (d-band) and graphite sp^2 carbon (G-band), respectively. The intensity ratio of the D and G bands (I_D/I_G) of Co NPs@SAs-NC is lower than that of Co NPs-NC. The XRD and Raman results show that Co NPs@SAs-NC has a higher

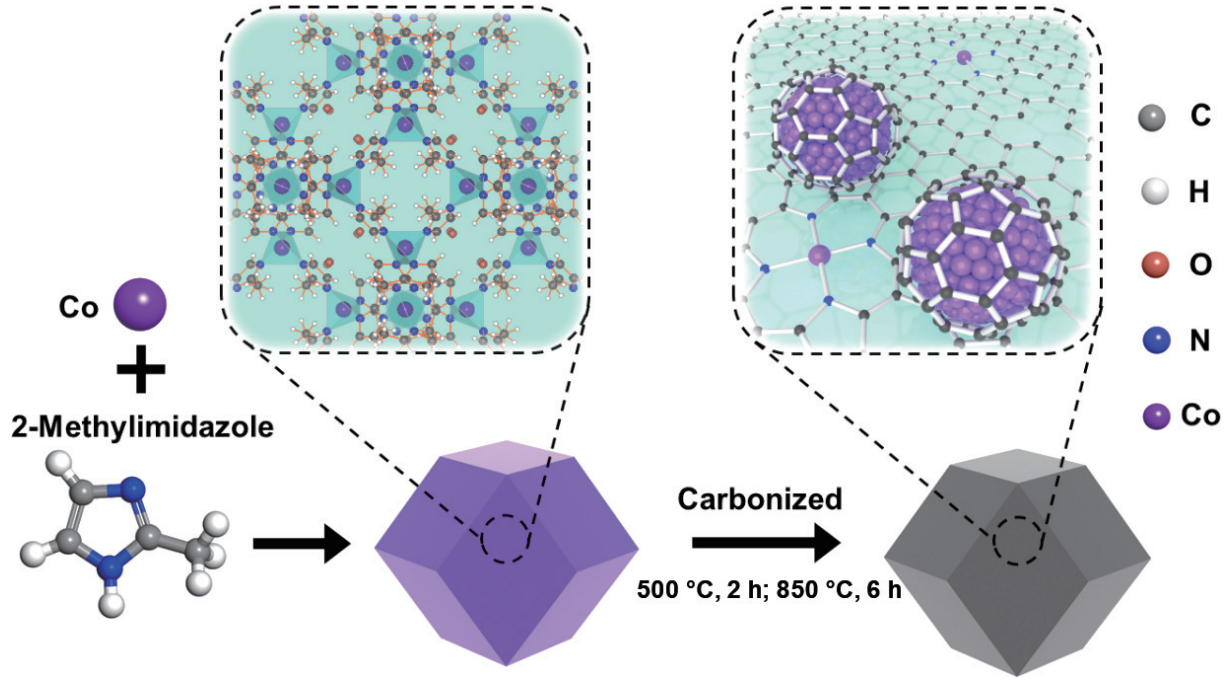

Figure 1 Schematic illustration of Co NPs@SAs-NC synthesis process.

graphitization degree which can improve the electrical conductivity and electrochemical catalytic activity of the catalysts.

The Brunauer–Emmett–Teller (BET) specific surface areas and porosities of the as-synthesized samples were analyzed by N_2 adsorption/desorption experiments at 77 K. According to Fig. S4 in the ESM, the N_2 adsorption/desorption isotherm of ZIF-67 is type I, while those of Co NPs@SAs-NC and Co NPs-NC are the combination of type I and type IV, reflecting the alteration of pore structure after calcination. The isotherms exhibit a marked increase in the N_2 uptake at a relatively low pressure ($P/P_0 < 0.01$), which indicates the presence of numerous micropores in samples. The BET surface areas of Co NPs@SAs-NC and Co NPs-NC are 525.1 and 483.8 $m^2 \cdot g^{-1}$, respectively. Furthermore, the pore volumes of Co NPs@SAs-NC and Co NPs-NC are calculated to 0.723 and 0.698 $cm^3 \cdot g^{-1}$, respectively. In addition, the pore size distribution curves obtained by the Barrett–Joyner–Halenda (BJH) method (Fig. S5 in the ESM) show a hierarchical porous structure that can enhance the surface-to-volume ratio and optimize the diffusion process to promote the HER reaction [41]. The inductively coupled plasma-optical emission spectroscopy (ICP-OES) result shows that the Co contents of Co NPs@SAs-NC and Co NPs-NC are 19.1 wt.% and 22.2 wt.% respectively.

The scanning electron microscopy (SEM) images of ZIF-67 indicate a regular dodecahedral morphology with a smooth surface (250 nm in size), and those of Co NPs@SAs-NC shows a wrinkled stereoscopic morphology (220 nm in size) (Figs. 2(a) and 2(b)). Therefore, the spatial structure of Co NPs@SAs-NC did not collapse, which facilitated the diffusion of water in the nanocatalyst. In addition, transmission electron microscopy (TEM) images were obtained for morphological analysis. As observed in Fig. 2(c), the sphere-like Co NPs (black dots) are uniformly scattered in the porous NC (gray substrate) derived from ZIF-67. The high-resolution TEM (HRTEM) image (Fig. 2(d)) shows that the Co NPs are completely encapsulated in the NC shell, indicating a close contact between Co lattice and Co SAs-doped NC surface. The average thickness of NC shell was measured to 2.3 nm (Fig. S6 in the ESM), which can prevent the aggregation of Co particles and won't hinder ion migration in the electrolyte [42]. Meanwhile, the fringe spacings were measured to be 0.21 and 0.36 nm, corresponding to the Co(111) and C(002) lattice planes, respectively [23, 43]. This result is consistent with the XRD peaks mentioned above. Besides, the atomic distribution of Co SAs in the carbon matrix can be observed in Figs. 2(e) and 2(f). Furthermore, the energy-dispersive X-ray spectroscopy (EDS) elemental mapping images (Fig. 2(g)) illustrate a uniform distribution of Co, C, and N, which is evidence of N doping. As a comparison, the Co NPs-NC is more distorted than Co NPs@SAs-NC shown in the SEM image (Fig. S7(a) in the ESM), but it still maintains the three-dimensional (3D) framework structures. TEM analyses of the Co NPs-NC show an incompact contact between the Co NPs and the NC shell (Figs. S7(b) and S7(c) in the ESM), and the EDS elemental mapping images show that most of the Co element exists as isolated Co particles (Fig. S7(d) in the ESM). The above TEM analyses prove that a proper isothermal process can promote the generation of single atoms and heterojunction between Co NPs and NC. The obtained Co SAs-doped NC shell can protect Co NPs from erosion during the electrochemical process, and Co NPs can be locked in the carbon matrix due to the strong interaction between Co SAs and Co NPs [11]. More importantly, the felicitous synergistic interaction between the Co NPs and Co SAs-doped NC shell may play a key role in improving the HER performance.

X-ray photoelectron spectroscopy (XPS) was performed to determine the valence states of Co NPs@SAs-NC. In the C 1s XPS spectrum (Fig. S8 in the ESM), the peaks at binding energies of 284.8, 285.5, 286.7 and 289.4 eV are assigned to the C–C/C=C, C–N, C=O and C–OH bonds, respectively [44]. In addition, the N 1s spectra indicate the presence of four N species (Fig. 3(a)), including graphitic N (401.2 eV), pyrrolic N (400.1 eV), pyridinic N (398.5 eV) and Co–N_x (399.3 eV) [45, 46]. Besides, the deconvolution of the Co 2p spectrum of Co NPs@SAs-NC provides three peaks at 778.7, 795.1 and 782.3 eV, which correspond to Co^0 $2p_{3/2}$, Co^0 $2p_{1/2}$ and Co–N_x coordination, respectively (Fig. 3(b)) [25]. Owing to inevitable surface oxidation, the oxidized Co peaks are detected at 780.5 ($2p_{3/2}$) and 796.8 eV ($2p_{1/2}$), respectively. As shown in Fig. S9 in the ESM, there is no visible Co–N_x peak in N 1s and Co 2p spectra of Co NPs-NC. Further insight into the interaction between the Co NPs and Co SAs-doped NC was obtained by performing X-ray absorption fine

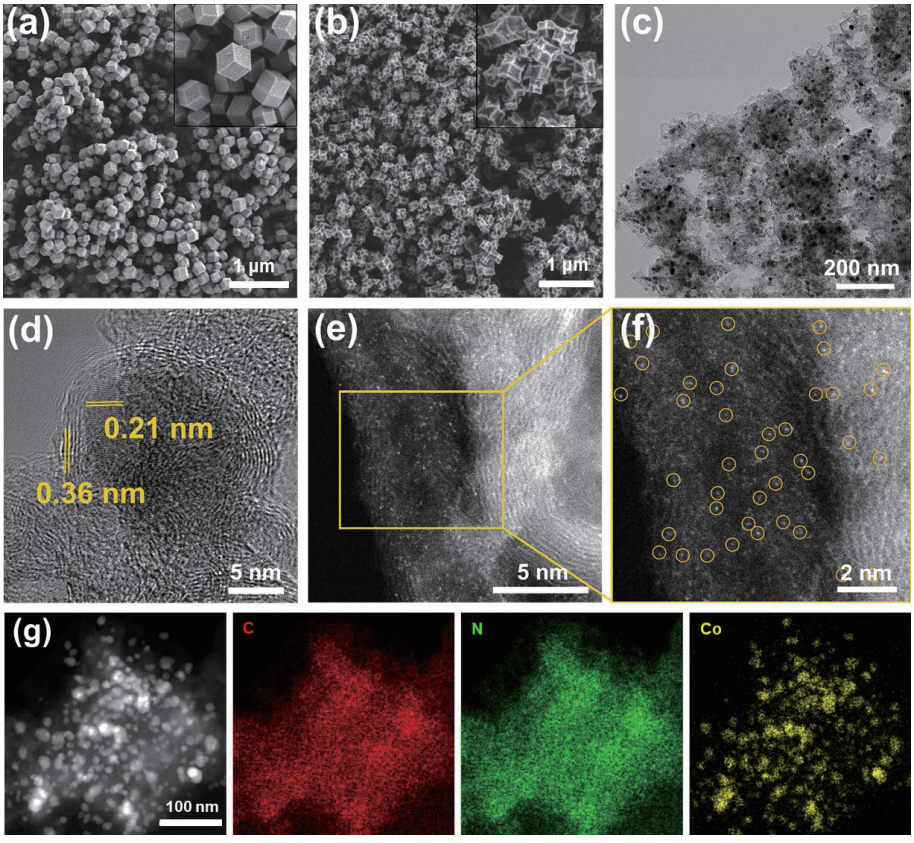

Figure 2 SEM images of (a) ZIF-67 and (b) Co NPs@SAs-NC. (c) and (d) TEM images of Co NPs@SAs-NC with different magnifications. (e) and (f) high-angle annular dark-field scanning TEM (HAADF-STEM) images showing the Co single atoms in the carbon matrix. (g) HADDF-STEM and elemental mapping images of Co, C and N of Co NPs-NC.

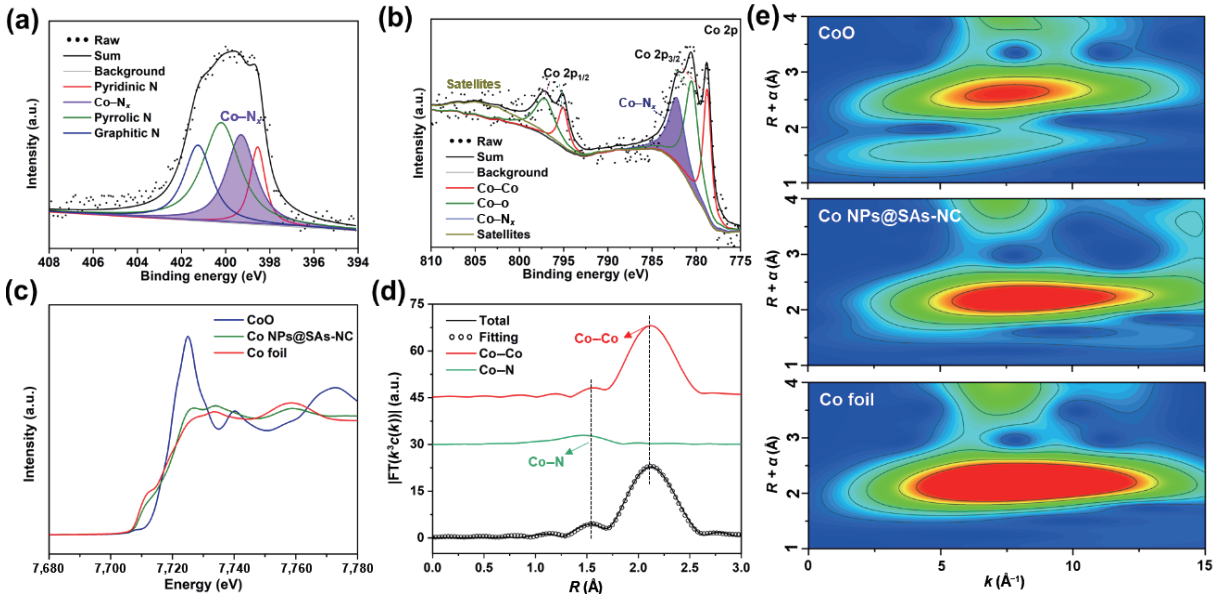

Figure 3 (a) N 1s and (b) Co 2p XPS spectra of Co NPs@SAs-NC. (c) The experimental Co K-edge XANES spectra of Co NPs@SAs-NC, Co foil and CoO. (d) The corresponding FT results of the EXAFS spectra of Co NPs@SAs-NC. Co K-edge EXAFS analysis of Co NPs@SAs-NC. Curves from top to bottom are the Co–Co and Co–N two-body backscattering signals χ2 included in the fit and the total signal superimposed on the experimental signal. The measured and calculated spectra show excellent agreement. (e) WT curves of Co NPs@SAs-NC, Co foil and CoO.

structure (XAFS) measurements. Figure 3(c) and Fig. S10 in the ESM present the Co K-edge X-ray absorption near edge structure (XANES) and extended X-ray absorption fine structure (EXAFS) curves of Co NPs@SAs-NC, respectively, with Co foil and CoO as references. The absorption edge of Co NPs@SAs-NC is located between those of Co foil and CoO, indicating that the valence state of Co element in Co NPs@SAs-NC is between Co^0 and Co^{2+} but close to Co^0. Furthermore, according to the Fourier transform (FT) of the Co K-edge EXAFS, the intensity maxima is 2.1 Å, corresponding to metallic Co–Co bonds, indicating that Co species is mainly present in the form of the elemental NPs in Co NPs@SAs-NC (Fig. 3(d)) [47]. However, a peak at approximately 1.5 Å is observed in the FT curve, which is attributed to Co–N_x coordination [48], and the coordination number of Co is approximately 4.2. To explore further the Co coordination of Co NPs@SAs-NC, wavelet transform (WT) of Co K-edge EXAFS was

carried out because it can show the intensities in both *k* and R space (Fig. 3(e)). Compared with the WT plots of Co foil and CoO standards, it can be observed that the intensity distribution of Co NPs@SAs-NC is similar to that of Co foil but the maximum intensity center of Co NPs@SAs-NC is slightly shifting to that of CoO in *k* space, revealing the wide dispersion of Co–Co and Co–N(O) bonding. The quantitative EXAFS analyses are shown in Table S1 in the ESM. From the results of TEM, XPS and XAFS, it can be concluded that Co species exist as the form of NPs (Co–Co) and SAs (Co–N_x) in the Co NPs@SAs-NC, respectively. And the electron transfer between Co NPs and Co–N_x may play a key role in enhancing the HER activity.

3.2 Electrocatalytic performance

The HER activity of the Co NPs@SAs-NC catalyst in an alkaline solution (1 M KOH) was investigated using a three-electrode system, and compared with those of commercial Pt/C, Co NPs-NC, and Co SAs-NC. The Co SAs-NC and NC were fabricated by etching Co NPs@SAs-NC and Co NPs-NC with 1M H_2SO_4 under hydrothermal conditions to eliminate Co NPs, respectively. As shown in Fig. S11 in the ESM, the Co NPs in the carbon matrix are completely removed. Besides, there is no Co^0 peak in XRD pattern and XPS spectra (Fig. S12 in the ESM). To prepare the working electrode, all the catalysts (in powder form) were dispersed in a mixed ethanol/water/Nafion solution followed by drop-casting onto the GCE surface. As shown in Fig. 4(a), the 20% Pt/C catalyst exhibits the highest HER activity with an overpotential (expressed henceforth as η_{10}) of 46 mV to reach a current density of 10 mA·cm^{-2}. Among the prepared catalysts, Co NPs@SAs-NC exhibits a remarkable catalytic performance toward HER with an η_{10} value of 110 mV, which is higher than those of most TM-based electrocatalysts in an alkaline solution (Table S2 in the ESM). However, the catalytic activities of Co NPs-NC and Co SAs-NC decrease significantly (the values of η_{10} are 193 and 526 mV, respectively), indicating Co NPs and SAs have the synergistic effects on HER reaction under the alkaline condition. To further understand the HER mechanism, the Tafel slope was obtained using the Tafel equation (η = blog$j$ + a) deduced from the polarization curve. The Tafel slope of 20% Pt/C is 31 mV·dec^{-1} (Fig. 4(b)), which is close to previously reported values [49, 50]. Meanwhile, the Tafel slope of Co NPs@SAs-NC (55 mV·dec^{-1}) is smaller than those of Co NPs-NC (64 mV·dec^{-1}), Co SAs-NC (169 mV·dec^{-1}), suggesting that the electrocatalytic kinetic of Co NPs@SAs-NC was more favorable for HER. Additionally, the durability of Co NPs@SAs-NC was tested using CV and long-term chronopotentiometry. As shown in Fig. 4(c), the polarization curve after 1,000 CV sweeps is like the initial one, and the *v*–*t* curve remains stable for 24 h, indicating that the SAs-doped NC shell protected the Co NPs from erosion during the electrochemical process. To further reveal the effect of Co–N_x sites in Co NPs@SAs-NC, we used phosphate to block the N sites by forming pyridinium (N-H) structure during the LSV process [51, 52]. As expected, Co NPs@SAs-NC exhibits poor catalytic activities with η_{10} values of 148 and 215 mV in 0.5 and 5 M H_3PO_4

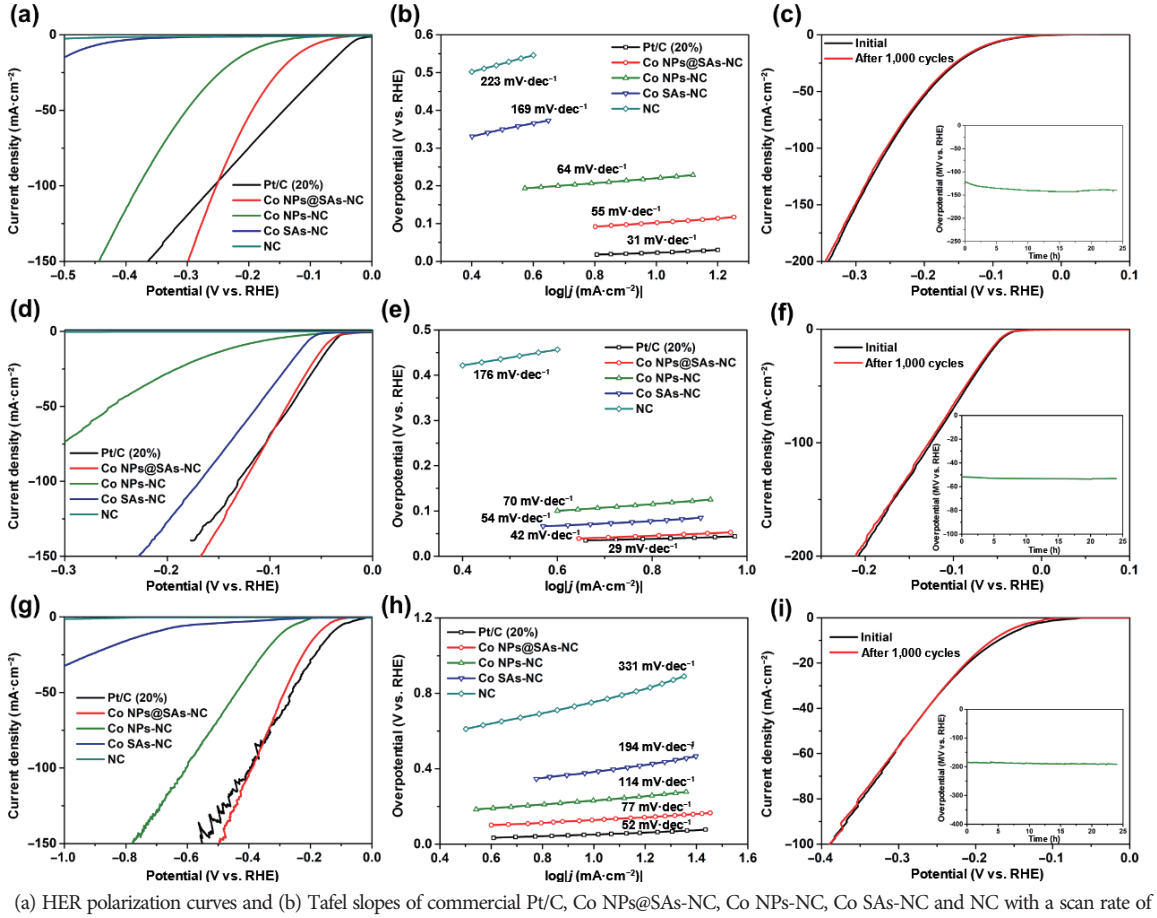

Figure 4 (a) HER polarization curves and (b) Tafel slopes of commercial Pt/C, Co NPs@SAs-NC, Co NPs-NC, Co SAs-NC and NC with a scan rate of 5 mV s^{-1} in 1.0 M KOH. (c) Polarization curves before and after 1,000 cycles and the chronopotentiometric curve with a constant current density of 10 mA·cm^{-2} for 24 h in 1.0 M KOH (inset of (c)). (d) HER polarization curves and (e) Tafel slopes of commercial Pt/C, Co NPs@SAs-NC, Co NPs-NC, Co SAs-NC and NC with a scan rate of 5 mV·s^{-1} in 0.5 M H_2SO_4. (f) Polarization curves of first and after 1,000 cycles and the chronopotentiometric curve with a constant current density of 10 mA·cm^{-2} for 24 h in 0.5 M H_2SO_4 (inset of (f)). (g) HER polarization curves and (h) Tafel slopes of commercial Pt/C, Co NPs@SAs-NC, Co NPs-NC, Co SAs-NC and NC with a scan rate of 5 mV·s^{-1} in 0.5 M PBS. (i) Polarization curves before and after 1,000 cycles and the chronopotentiometric curve with a constant current density of 10 mA·cm^{-2} for 24 h in 0.5 M PBS (inset of (i)). All HER polarization curves were *iR*-corrected.

solutions, respectively (Fig. S13 in the ESM), demonstrating the critical role of the Co–N_x site in the HER process. The double-layer capacitances (C_{dl}) can be obtained by the CV tests with scanning rates from 10 to 50 mV·s^{-1}. The C_{dl} of the Co NPs@SAs-NC is higher than those of Co-NPs-NC and Co-SAs-NC (Fig. S14 in the ESM), indicating that Co NPs@SAs-NC has the largest active area in three Co-based catalysts.

The HER activity of Co NPs@SAs-NC catalyst in an acidic solution (0.5 M H_2SO_4) was also performed. As shown in Fig. 4(d), the commercial 20% Pt/C exhibits the best actives with 41 mV overpotential at 10 mA·cm^{-2} current density and 29 mV·dec^{-1} of Tafel slope (Fig. 4(e)). The Co NPs@SAs-NC shows a better performance with 47 mV overpotential at 10 mA·cm^{-2} than Co NPs-NC (η_{10} = 132 mV) and Co SAs-NC (η_{10} = 67 mV). The HER activity of Co NPs@SAs-NC is higher than those of most noble-free TM electrocatalysts in the acidic solutions (Table S3 in the ESM). The Tafel slope of Co NPs@SAs-NC was calculated to 42 mV·dec^{-1}, compared with Co NPs-NC (70 mV·dec^{-1}) and Co SAs-NC (54 mV·dec^{-1}). The Tafel slope result indicates that the catalytic activities of Co NPs@SAs-NC toward HER follow the Volmer–Heyrovsky mechanism in 0.5 M H_2SO_4 [53]. After 1,000 cycles of long-term CV test, there is a negligible reduction of current density compared with the first cycle (Fig. 4(f)). The double-layer capacitances (C_{dl}) data of Co NPs@SAs-NC in 0.5 M H_2SO_4 are displayed in Fig. S15 in the ESM, and the C_{dl} value of Co NPs@SAs-NC is the highest in the three Co-based nanocatalysts under the acidic condition.

We also evaluated the HER performances of Co NPs@SAs-NC catalyst in neutral electrolytes (0.5 M PBS), and the result is shown in Figs. 4(g)–4(i). The overpotentials at 10 mA·cm^{-2} current density of Pt/C, Co NPs@SAs-NC, Co NPs-NC and Co SAs-NC are 128, 171, 316 and 707 mV respectively (Fig. 4(f)). The Tafel slope of Pt/C was calculated to 52 mV·dec^{-1} which is corresponding to the reported results [54]; the Co NPs@SAs-NC (77 mV·dec^{-1}) shows a better performance than Co NPs-NC (114 mV·dec^{-1}) and Co SAs-NC (194 mV·dec^{-1}) (Fig. 4(f)). The stability of Co NPs@SAs-NC in neutral media was evaluated by 100 cycles of long-term CV test. Compare with the first cycle there is a negligible reduction of current density after 1,000 CV cycles (Fig. 4(f)). The double-layer capacitances (C_{dl}) results of Co NPs@SAs-NC in 0.5 M PBS are displayed in Fig. S16 in the ESM and the C_{dl} value was calculated to 25.32 mF·cm^{-2}, which is higher than those of Co NPs-NC (8.73 mF·cm^{-2}) and Co SAs-NC (7.51 mF·cm^{-2}).

The characterization of Co NPs@SAs-NC after HER test demonstrates well-matched phase and valence states from XRD (Fig. S17(a) in the ESM) and XPS resultd (Fig. S17(b)–S17(d) in the ESM) and the morphology maintains well from TEM images (Fig. S18 in the ESM), further suggesting the superb stability.

In general, the catalytic performances of Co NPs@SAs-NC toward HER in acidic, alkaline, and neutral media are the best among three Co-based catalysts, revealing the synergy between the Co NPs and Co SAs-doped NC. The sample NC without Co species shows a poor catalytic performance (Fig. 4), implying that the N-doped carbon matrix has few contributions to catalytic activity.

3.3 DFT calculations

To investigate the synergy between the Co NPs and Co SAs-doped NC, we employed DFT calculations to obtain the electronic structures and energy changes of Co NPs-NC, Co SAs-NC and Co NPs@SAs-NC. As shown in Fig. 5(a) and Figs. S19–S21 in the ESM, the Co NPs@SAs heterointerface model was constructed using Co–N_4 single-layered graphene and the Co(111) plane because the peak intensity of Co(111) is higher than that of Co(200) in the XRD pattern, and the lattice fringe of Co(111) is observed in the HRTEM image. The Co–N_4 model was composed by substituting four pyridinic N atoms bonded with one Co atom for C atoms in graphene model. The charge density difference images show strong electron transfer from the Co superlattice to Co single atom (Fig. 5(b)), and the quantity of transferred electron is 0.1 e^- via Bader charge analysis (Table S4 in the ESM). Besides, the partial density of states (pDOS) data show that the DOS of Co single atoms near the Fermi level is mainly originated from the d state. Meanwhile, the calculated d-band centers of Co single atom

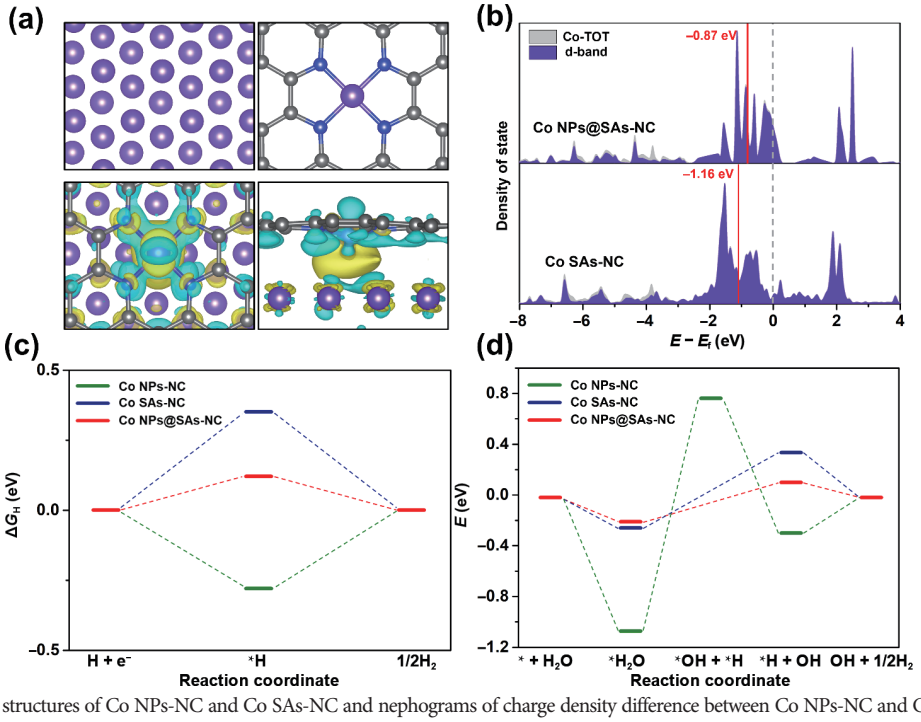

Figure 5 (a) Optimized structures of Co NPs-NC and Co SAs-NC and nephograms of charge density difference between Co NPs-NC and Co SAs-NC. (b) PDOS of Co-TOT (gray line) and d-band (purple line); red lines show the centers of Co d-band. Free energies of the HER process in (c) acidic and (d) alkaline conditions for different models.

relative to the Fermi level are −0.87 eV (Co NPs@SAs-NC) and −1.16 eV (Co SAs-NC) (Fig. 5(c)), respectively. These results indicate that the Co single atom of Co NPs@SAs-NC has a stronger electronic attraction, thereby increasing the charge density of Co single atoms and balancing the adsorption and desorption of H atoms [55]. The HER activity of a catalyst in the acidic solution is typically described by the Gibbs free energy of the intermediate H adsorption (ΔG_H), and a low value of $|\Delta G_H|$ is desirable. The calculation results indicate that the H atoms are adsorbed in the top position of Co single atom in the Co NPs@SAs-NC and Co SAs-NC, whereas adsorbed in the hollow position of Co atoms in the Co NPs-NC (Fig. S22 in the ESM). As shown in Fig. 5(d), the ΔG_H corresponding to the Co NPs@SAs is approximately 0.12 eV, which is much closer to 0 than those of Co SAs (0.35 eV) and Co NPs (−0.38 eV), indicating that the Co NPs@SAs executed thermo-neutral adsorption of protons to improve the HER activity. Considering the favorable pathways on three models under the alkaline condition (Figs. S23–S25 in the ESM), the Co NPs@SAs model is more thermodynamically favorable than Co NPs and Co SAs (Fig. 5(e)). Generally, the H_2O molecular can be adsorbed appropriately via Co–H bond in Co SAs and Co NPs@SAs, and then directly dissociated, while the H_2O molecular is adsorbed via Co–O bond in Co NPs. In addition, the adsorption energy of H_2O on Co NPs (−1.05 eV) is much lower than those on Co SAs (−0.24 eV), indicating that the Co nanoparticles may enrich and activate water molecules and promote the water splitting process.

4 Conclusion

In summary, Co NPs and SAs encapsulated in N-doped porous carbon (Co NPs@SAs-NC) were successfully synthesized via a facile carbonization process using ZIF-67 as a sacrificial precursor. The segmented calcination method contributes to the co-existence and homogeneous distribution of Co NPs and SAs. The Co NPs@SAs-NC exhibits prominent electrocatalytic activities toward HER with an overpotential of 110 mV in the alkaline solution, 47 mV in the acidic solution and 171 mV in the neutral solution to reach a current density of 10 $mA{\cdot}cm^{-2}$. Because of the protection of the carbon shell, it still retains its stability after an uninterrupted chronopotentiometry test is performed for 24 h. According to the experiment tests and DFT calculations, the HER performance is improved by the synergistic effect of Co NPs and Co–N_4 sites. This work provides an insight into the synergistic effect between the TM NPs and SAs-doped carbon materials and offers a viable synthetic scheme to obtain NPs@SAs catalysts.

Acknowledgements

This work was supported by the National Key Research and Development Program of China (No. 2017YFB0403401). The authors gratefully acknowledge the financial support from the China Postdoctoral Science Foundation (Nos. 2021M691759, and 2021TQ0169). This work was supported by Beijing Natural Science Foundation (No. 2224103). We thank the BL11B station at the Shanghai Synchrotron Radiation Facility and the 1W1B and 4B7A stations at the Beijing Synchrotron Radiation Facility.

Electronic Supplementary Material: Supplementary material is available in the online version of this article at https://doi.org/10.1007/s12274-022-4448-6.

References

[1] 1] Chu, S.; Majumdar, A. Opportunities and challenges for a sustainable energy future. *Nature* **2012**, *488*, 294–303.
[2] Chornet, E.; Czernik, S. Harnessing hydrogen. *Nature* **2002**, *418*, 928–929.
[3] Zhang, J. N.; Hu, W. P.; Cao, S.; Piao, L. Recent progress for hydrogen production by photocatalytic natural or simulated seawater splitting. *Nano Res.* **2020**, *13*, 2313–2322.
[4] Davoodabadi, A.; Mahmoudi, A.; Ghasemi, H. The potential of hydrogen hydrate as a future hydrogen storage medium. *iScience* **2021**, *24*, 101907.
[5] Yu, Z. Y.; Duan, Y.; Feng, X. Y.; Yu, X. X.; Gao, M. R.; Yu, S. H. Clean and affordable hydrogen fuel from alkaline water splitting: Past, recent progress, and future prospects. *Adv. Mater.* **2021**, *33*, 2007100.
[6] Yukesh Kannah, R.; Kavitha, S.; Preethi; Parthiba Karthikeyan, O.; Kumar, G.; Dai-Viet, N. V.; Rajesh Banu, J. Techno-economic assessment of various hydrogen production methods—A review. *Bioresour. Technol.* **2021**, *319*, 124175.
[7] Wang, S.; Lu, A. L.; Zhong, C. J. Hydrogen production from water electrolysis: Role of catalysts. *Nano Converg.* **2021**, *8*, 4.
[8] Mahmood, J.; Li, F.; Jung, S. M.; Okyay, M. S.; Ahmad, I.; Kim, S. J.; Park, N.; Jeong, H. Y.; Baek, J. B. An efficient and pH-universal ruthenium-based catalyst for the hydrogen evolution reaction. *Nat. Nanotechnol.* **2017**, *12*, 441–446.
[9] Chen, G. B.; Wang, T.; Zhang, J.; Liu, P.; Sun, H. J.; Zhuang, X. D.; Chen, M. W.; Feng, X. L. Accelerated hydrogen evolution kinetics on NiFe-layered double hydroxide electrocatalysts by tailoring water dissociation active sites. *Adv. Mater.* **2018**, *30*, 1706279.
[10] Fang, S.; Zhu, X. R.; Liu, X. K.; Gu, J.; Liu, W.; Wang, D. H.; Zhang, W.; Lin, Y.; Lu, J. L.; Wei, S. Q. et al. Uncovering near-free platinum single-atom dynamics during electrochemical hydrogen evolution reaction. *Nat. Commun.* **2020**, *11*, 1029.
[11] Liang, L. H.; Jin, H. H.; Zhou, H.; Liu, B. S.; Hu, C. X.; Chen, D.; Wang, Z.; Hu, Z. Y.; Zhao, Y. F.; Li, H. W. et al. Cobalt single atom site isolated pt nanoparticles for efficient ORR and HER in acid media. *Nano Energy* **2021**, *88*, 106221.
[12] Wang, Y.; Zheng, X. B.; Wang, D. S. Design concept for electrocatalysts. *Nano Res.* **2022**, *15*, 1730–1752.
[13] Gong, M.; Dai, H. J. A mini review of NiFe-based materials as highly active oxygen evolution reaction electrocatalysts. *Nano Res.* **2015**, *8*, 23–39.
[14] Zhong, H. X.; Wang, J.; Zhang, Q.; Meng, F. L.; Bao, D.; Liu, T.; Yang, X. Y.; Chang, Z. W.; Yan, J. M.; Zhang, X. B. In situ coupling FeM (M = Ni, Co) with nitrogen-doped porous carbon toward highly efficient trifunctional electrocatalyst for overall water splitting and rechargeable Zn-air battery. Adv. Sustain. *Syst.* **2017**, *1*, 1700020.
[15] Liu, G.; He, D. Y.; Yao, R.; Zhao, Y.; Li, J. P. Amorphous NiFeB nanoparticles realizing highly active and stable oxygen evolving reaction for water splitting. *Nano Res.* **2018**, *11*, 1664–1675.
[16] Pang, L. W.; Liu, W.; Zhao, X. R.; Zhou, M.; Qin, J. Y.; Yang, J. Engineering electronic structures of nickel cobalt phosphide via iron doping for efficient overall water splitting. *Chemelectrochem* **2020**, *7*, 4913–4921.
[17] Wu, J. B.; Xiong, L. K.; Zhao, B. T.; Liu, M. L.; Huang, L. Densely populated single atom catalysts. *Small Methods* **2020**, *4*, 1900540.
[18] Cheng, H.; Liu, Q.; Diao, Y. W.; Wei, L. L.; Chen, J. H.; Wang, F. X. $CoMo_2S_4$ with superior conductivity for electrocatalytic hydrogen evolution: Elucidating the key role of Co. *Adv. Funct. Mater.* **2021**, *31*, 2103732.
[19] Zheng, J. G.; Xu, A. N.; Wu, A. J.; Li, X. D. Plasma-engraved Co_2N nanostructures toward high-performance alkaline hydrogen evolution. *ACS Appl. Mater. Interfaces* **2021**, *13*, 21231–21240.
[20] Jing, H. Y.; Zhu, P.; Zheng, X. B.; Zhang, Z. D.; Wang, D. S.; Li, Y. D. Theory-oriented screening and discovery of advanced energy transformation materials in electrocatalysis. *Adv. Powder Mater.* **2022**, *1*, 100013.
[21] Tahir, M.; Mahmood, N.; Zhang, X. X.; Mahmood, T.; Butt, F. K.; Aslam, I.; Tanveer, M.; Idrees, F.; Khalid, S.; Shakir, I. et al. Bifunctional catalysts of Co_3O_4@GCN tubular nanostructured (TNS) hybrids for oxygen and hydrogen evolution reactions. *Nano Res.* **2015**, *8*, 3725–3736.

[22] Wang, J.; Kong, H.; Zhang, J. Y.; Hao, Y.; Shao, Z. P.; Ciucci, F. Carbon-based electrocatalysts for sustainable energy applications. *Prog. Mater. Sci.* **2021**, *116*, 100717.
[23] Huang, L.; Zhang, X. P.; Han, Y. J.; Wang, Q. Q.; Fang, Y. X.; Dong, S. J. . *In situ* synthesis of ultrathin metal-organic framework nanosheets:A new method for 2d metal-based nanoporous carbon electrocatalysts. *J. Mater. Chem. A* **2017**, *5*, 18610–18617.
[24] Liu, Y. Y.; Han, G. S.; Zhang, X. Y.; Xing, C. C.; Du, C. X.; Cao, H. Q.; Li, B. J. Co-Co_3O_4@carbon core–shells derived from meta-organic framework nanocrystals as efficient hydrogen evolution catalysts. *Nano Res.* **2017**, *10*, 3035–3048.
[25] Jiang, R.; Wang, W. Z.; Zheng, X.; Li, Q.; Xu, Z. M.; Peng, J. Hierarchically porous CoP@CNR nanorod derived from metal-organic frameworks as noble-metal-free catalyst for dehydrogenization of ammonia-borane. *Int. J. Hydrogen Energy* **2021**, *46*, 5345–5354.
[26] Wang, A. Q.; Li, J.; Zhang, T. Heterogeneous single-atom catalysis. *Nat. Rev. Chem.* **2018**, *2*, 65–81.
[27] Sun, T. T.; Zhao, S.; Chen, W. X.; Zhai, D.; Dong, J. C.; Wang, Y.; Zhang, S. L.; Han, A. J.; Gu, L.; Yu, R. et al. Single-atomic cobalt sites embedded in hierarchically ordered porous nitrogen-doped carbon as a superior bifunctional electrocatalyst. *Proc. Natl. Acad. Sci. USA* **2018**, *115*, 12692–12697.
[28] Sun, T. T.; Zhang, P. P.; Chen, W. X.; Wang, K.; Fu, X. Z.; Zheng, T. Y.; Jiang, J. Z. Single iron atoms coordinated to g-C_3N_4 on hierarchical porous n-doped carbon polyhedra as a high-performance electrocatalyst for the oxygen reduction reaction. *Chem. Commun.* **2020**, *56*, 798–801.
[29] Chen, Y. J.; Gao, R.; Ji, S. F.; Li, H. J.; Tang, K.; Jiang, P.; Hu, H. B.; Zhang, Z. D.; Hao, H. G.; Qu, Q. Y. et al. Atomic-level modulation of electronic density at cobalt single-atom sites derived from metal-organic frameworks: Enhanced oxygen reduction performance. *Angew. Chem., Int. Ed.* **2021**, *60*, 3212–3221.
[30] Cui, T. T.; Wang, Y. P.; Ye, T.; Wu, J.; Chen, Z. Q.; Li, J.; Lei, Y. P.; Wang, D. S.; Li, Y. D. Engineering dual single-atom sites on 2D ultrathin N-doped carbon nanosheets attaining ultra-low-temperature zinc-air battery. *Angew. Chem. , Int. Ed.* **2022**, *61*, e202115219.
[31] Morales-Guio, C. G.; Stern, L. A.; Hu, X. L. Nanostructured hydrotreating catalysts for electrochemical hydrogen evolution. *Chem. Soc. Rev.* **2014**, *43*, 6555–6569.
[32] Nørskov, J. K.; Bligaard, T.; Logadottir, A.; Kitchin, J. R.; Chen, J. G.; Pandelov, S.; Stimming, U. Trends in the exchange current for hydrogen evolution. *J. Electrochem. Soc.* **2005**, *152*, J23.
[33] Wang, Y.; Zheng, M.; Li, Y. R.; Ye, C. L.; Chen, J.; Ye, J. Y.; Zhang, Q. H.; Li, J.; Zhou, Z. Y.; Fu, X. Z. et al. P-d orbital hybridization induced by a monodispersed ga site on a Pt_3Mn nanocatalyst boosts ethanol electrooxidation. *Angew. Chem., Int. Ed.* **2022**, *61*, e202115735.
[34] Yang, J. R.; Li, W. H.; Xu, K. N.; Tan, S. D.; Wang, D. S.; Li, Y. D. Regulating the tip effect on single-atom and cluster catalysts: Forming reversible oxygen species with high efficiency in chlorine evolution reaction. *Angew. Chem., Int. Ed.* **2022**, *61*, e202200366.
[35] Chen, Z. L.; Qing, H. L.; Zhou, K.; Sun, D. L.; Wu, R. B. Metal-organic framework-derived nanocomposites for electrocatalytic hydrogen evolution reaction. *Prog. Mater. Sci.* **2020**, *108*, 100618.
[36] Sun, T. T.; Xu, L. B.; Wang, D. S.; Li, Y. D. Metal organic frameworks derived single atom catalysts for electrocatalytic energy conversion. *Nano Res.* **2019**, *12*, 2067–2080.
[37] Wang, W. Z.; Dai, Z. W.; Jiang, R.; Li, Q.; Zheng, X.; Liu, W.; Luo, Z. G.; Xu, Z. M.; Peng, J. Highly phosphatized magnetic catalyst with electron transfer induced by quaternary synergy for efficient dehydrogenation of ammonia borane. *ACS Appl. Mater. Interfaces* **2020**, *12*, 43854–43863.
[38] Shen, K.; Chen, X. D.; Chen, J. Y.; Li, Y. W. Development of mof-derived carbon-based nanomaterials for efficient catalysis. *ACS Catal.* **2016**, *6*, 5887–5903.
[39] Han, A. J.; Wang, B. Q.; Kumar, A.; Qin, Y. J.; Jin, J.; Wang, X. H.; Yang, C.; Dong, B.; Jia, Y.; Liu, J. F. et al. Recent advances for MOF-derived carbon-supported single-atom catalysts. *Small Methods* **2019**, *3*, 1800471.
[40] Feng, L.; Wang, K. Y.; Day, G. S.; Ryder, M. R.; Zhou, H. C. Destruction of metal-organic frameworks: Positive and negative aspects of stability and lability. *Chem. Rev.* **2020**, *120*, 13087–13133.
[41] Cai, G. R.; Yan, P.; Zhang, L. L.; Zhou, H. C.; Jiang, H. L. Metal-organic framework-based hierarchically porous materials: Synthesis and applications. *Chem. Rev.* **2021**, *121*, 12278–12326.
[42] Sun, H.; Lian, Y. B.; Yang, C.; Xiong, L. B.; Qi, P. W.; Mu, Q. Q.; Zhao, X. H.; Guo, J.; Deng, Z.; Peng, Y. A hierarchical nickel-carbon structure templated by metal-organic frameworks for efficient overall water splitting. *Energy Environ. Sci.* **2018**, *11*, 2363–2371.
[43] Xia, B. Y.; Yan, Y.; Li, N.; Wu, H. B.; Lou, X. W.; Wang, X. A metal-organic framework-derived bifunctional oxygen electrocatalyst. *Nat. Energy* **2016**, *1*, 15006.
[44] Chen, L.; Chen, Z.; Liu, X. D.; Wang, X. L. Bimetallic metal-organic framework derived doped carbon nanostructures as high-performance electrocatalyst towards oxygen reactions. *Nano Res.* **2021**, *14*, 1533–1540.
[45] Xie, Y. H.; Chen, Y.; Liu, L.; Tao, P.; Fan, M. P.; Xu, N.; Shen, X. W.; Yan, C. L. Ultra-high pyridinic N-doped porous carbon monolith enabling high-capacity K-ion battery anodes for both half-cell and full-cell applications. *Adv. Mater.* **2017**, *29*, 1702268.
[46] Mahsud, A.; Chen, J. N.; Yuan, X. L.; Lyu, F.; Zhong, Q. X.; Chen, J. X.; Yin, Y. D.; Zhang, Q. Self-templated formation of cobalt-embedded hollow N-doped carbon spheres for efficient oxygen reduction. *Nano Res.* **2021**, *14*, 2819–2825.
[47] Yin, P. Q.; Yao, T.; Wu, Y. E.; Zheng, L. R.; Lin, Y.; Liu, W.; Ju, H. X.; Zhu, J. F.; Hong, X.; Deng, Z. X. et al. Single cobalt atoms with precise N-coordination as superior oxygen reduction reaction catalysts. *Angew. Chem., Int. Ed.* **2016**, *55*, 10800–10805.
[48] Wang, X. Q.; Chen, Z.; Zhao, X. Y.; Yao, T.; Chen, W. X.; You, R.; Zhao, C. M.; Wu, G.; Wang, J.; Huang, W. X. et al. Regulation of coordination number over single co sites: Triggering the efficient electroreduction of CO_2. *Angew. Chem., Int. Ed.* **2018**, *57*, 1944–1948.
[49] Wang, X.; Yang, Z.; Si, W. Y.; Shen, X. Y.; Li, X. D.; Li, R.; Lv, Q.; Wang, N.; Huang, C. S. Cobalt-nitrogen-doped graphdiyne as an efficient bifunctional catalyst for oxygen reduction and hydrogen evolution reactions. *Carbon* **2019**, *147*, 9–18.
[50] Yan, L. T.; Jiang, H. M.; Xing, Y. L.; Wang, Y.; Liu, D. D.; Gu, X.; Dai, P. C.; Li, L. J.; Zhao, X. B. Nickel metal-organic framework implanted on graphene and incubated to be ultrasmall nickel phosphide nanocrystals acts as a highly efficient water splitting electrocatalyst. *J. Mater. Chem. A* **2018**, *6*, 1682–1691.
[51] Li, O. L.; Prabakar, K.; Kaneko, A.; Park, H.; Ishizaki, T. Exploration of lewis basicity and oxygen reduction reaction activity in plasma-tailored nitrogen-doped carbon electrocatalysts. *Catal. Today* **2019**, *337*, 102–109.
[52] Li, X. G.; Popov, B. N.; Kawahara, T.; Yanagi, H. Non-precious metal catalysts synthesized from precursors of carbon, nitrogen, and transition metal for oxygen reduction in alkaline fuel cells. *J. Power Sources* **2011**, *196*, 1717–1722.
[53] Pentland, N.; Bockris, J. O. M.; Sheldon, E. Hydrogen evolution reaction on copper, gold, molybdenum, palladium, rhodium, and iron: Mechanism and measurement technique under high purity conditions. *J. Electrochem. Soc.* **1957**, *104*, 182–194.
[54] Yoon, H.; Song, H. J.; Ju, B.; Kim, D. W. Cobalt phosphide nanoarrays with crystalline-amorphous hybrid phase for hydrogen production in universal-pH. *Nano Res.* **2020**, *13*, 2469–2477.
[55] Yang, Q.; Liu, H. X.; Yuan, P.; Jia, Y.; Zhuang, L. Z.; Zhang, H. W.; Yan, X. C.; Liu, G. H.; Zhao, Y. F.; Liu, J. Z. et al. Single carbon vacancy traps atomic platinum for hydrogen evolution catalysis. *J. Am. Chem. Soc.* **2022**, *144*, 2171–2178.